Jet mixing optimization using Event-Based Imaging Velocimetry

Luca Franceschelli[1], Enrico Amico[2], Christian E. Willert[3], Marco Raiola[1], Gioacchino Cafiero[2] and Stefano Discetti[1]

1: Department of Aerospace Engineering, Universidad Carlos III de Madrid, Avda. Universidad 30, Leganés, 28911, Madrid, Spain
2: Department of Mechanical and Aerospace Engineering, Politecnico di Torino, Corso Duca degli Abruzzi 24, Turin, 10129, Italy
3: DLR Institute of Propulsion Technology, German Aerospace Center, Linder Höhe, Köln, 51170, Germany
*Corresponding author: lfrances@ing.uc3m.es

Keywords: Event-based imaging velocimetry, jet flow, flow control, mixing enhancement, synthetic jets.

ABSTRACT

This contribution investigates the use of pulsed Event-Based Imaging Velocimetry (EBIV) as an in-the-loop sensor for experimental optimisation of open-loop control of a turbulent round jet. By leveraging the low latency, high dynamic range, and reduced data rate of event-based vision sensors under pulsed illumination, EBIV enables time-resolved planar velocity measurements with low-cost, non-intrusive instrumentation. The resulting spatially resolved velocity fields are used to define a mixing-related reward based on the turbulent kinetic energy averaged over a region of interest, enabling rapid evaluation of candidate forcing inputs beyond what is typically feasible with probe-based sensing. A Bayesian optimisation strategy is employed to tune the actuation parameters of six azimuthally distributed synthetic jets, while symmetry constraints are imposed to preserve observability in the EBIV measurement plane. The optimisation produces a consistent increase of the EBIV-derived reward and reveals clear performance trends with respect to the actuation Strouhal numbers and phase delays. The time-resolved planar fields enable a flow-physics analysis of the best-performing cases through mean-flow statistics, jet spreading and centreline decay, the coherent structures extracted by Proper Orthogonal Decomposition, and a low-dimensional embedding of the explored actuation space. Notably, defining the reward on the spatially averaged Turbulent Kinetic Energy decouples mixing enhancement from centreline-velocity decay, the latter being the surrogate commonly maximised by conventional jet-control optimisation. Volumetric 3D particle-tracking velocimetry is used only for an instantaneous, qualitative cross-check of the three-dimensional vortical organisation, with a systematic volumetric analysis left to future work.

1. Introduction

Jet flows are common in aerospace and industrial systems, where mixing, noise, and performance depend on their unsteady dynamics. Their control and optimization has usually relied on intrusive single-point sensors (e.g., hot-wires and pressure transducers) that provide kilohertz-rate

signals but limited access to global flow organisation (Parekh et al., 1996; Zhou et al., 2020). Conversely, optical velocimetry such as Particle Image Velocimetry (PIV) can capture the relevant flow structures in velocity and vorticity fields, but the associated data rates, hardware cost, and post-processing demands typically make it impractical for evaluating large numbers of candidate control laws.

Event-Based Imaging Velocimetry (EBIV) offers a sensing workflow that combines high effective temporal resolution with reduced data rate and latency by exploiting the asynchronous output and high dynamic range of event-based vision sensors (Gallego et al., 2022). When combined with pulsed illumination, pulsed-EBIV further improves robustness by synchronising event acquisition with controlled light pulses (Willert, 2023). This enables rapid reconstruction of planar velocity fields and, crucially, the computation of flow-based reward metrics at a throughput compatible with iterative optimization.

In this study, EBIV is used as an in-the-loop diagnostic and evaluation tool for open-loop optimization of a turbulent round jet actuated by six azimuthally distributed synthetic-jets (SJs). A Bayesian Optimization (BO) strategy iteratively explores actuation parameters to maximise a reward derived from the EBIV velocity fields, defined here from the spatially averaged Turbulent Kinetic Energy (TKE) within a region of interest. To support physical interpretation and to cross-check three-dimensional effects not observable in planar measurements, the optimised responses are additionally examined qualitatively using volumetric 3D particle tracking velocimetry (Shake-the-Box). Overall, the approach targets scalable experimental optimization with spatially informed objectives, without the cost and processing burden of high-speed PIV.

2. Experimental setup

2.1. Jet facility and EBIV setup

An overview of the experimental rig and the EBIV-based optimisation workflow is shown in Figure 1. Experiments are conducted in the air-jet facility located in the anechoic chamber at Universidad Carlos III de Madrid (Moreno et al., 2024). A round jet issues from a nozzle of exit diameter $D = 20\,\mathrm{mm}$; a tripping device at the beginning of the contraction promotes a turbulent boundary layer at the nozzle exit. The flow is seeded with $1\,\mu\mathrm{m}$ Di-Ethyl-Hexyl-Sebacate (DEHS) droplets supplied by a controlled mixture of clean and seeded air, ensuring approximately constant total mass flow rate and seeding density throughout the campaign.

Illumination is provided by a low-cost laser module (LaserTree LT-4LDS-V2) shaped into a $\sim 1\,\mathrm{mm}$-thick light sheet aligned with the jet midplane and operated in pulsed mode. The laser is pulsed at a frequency $f = 1500$ Hz, with a duty cycle of 15%, corresponding to a pulse width of $\Delta t = 100\mu$s, providing time-resolved sequences. Velocity measurements are acquired using a Prophesee EVK-4 Event-Based Vision (EBV) camera (IMX636, 1280×720 px), in the white circle in Figure 1 - left, whose internal biases have been configured to suppress negative events and maximize bandwidth

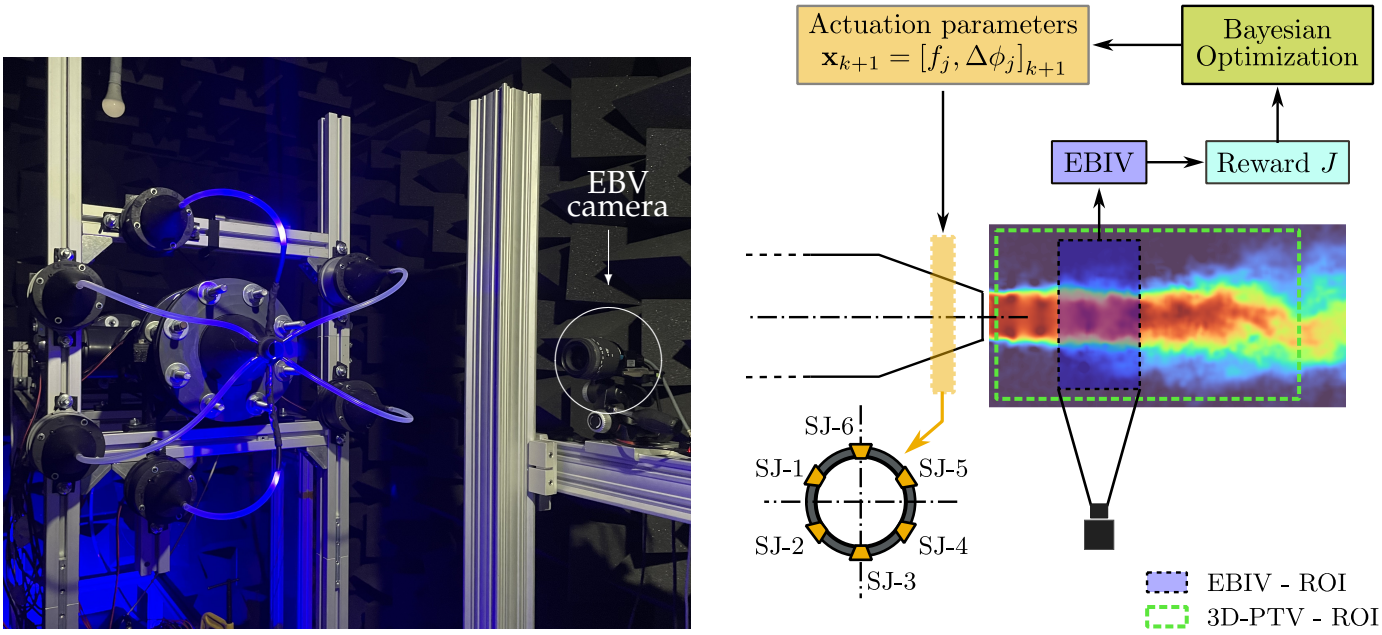

Figure 1. Experimental set-up (left) showing the jet facility and event-based camera, and corresponding EBIV-based control architecture (right) implemented for jet flow control experiments.

for positive-only events. A 50 mm lens provides a spatial resolution of ≈ 19.3 px/mm and a field of view of $\approx 3.3 \times 1.8\, D^2$, with $f_\# = 4.6$. The laser is driven by a square-wave signal that also triggers the camera stream, enabling synchronisation of illumination and event acquisition. A dedicated workstation performs acquisition, online processing, and the optimisation loop.

2.2. Actuation

The jet is forced by six azimuthally distributed SJ actuators located 1D upstream of the nozzle exit. The actuators are labelled SJ-1 to SJ-6 according to the azimuthal arrangement shown in Figure 1; this numbering is used throughout the paper to identify the independently driven forcing units. Actuation signals are generated by a National Instruments CompactRIO (cRIO) system and amplified before driving the actuators. The actuation amplitude is selected to maintain an approximately constant effective ejection velocity U_0 across actuation frequencies, defined from the phase-averaged centreline velocity during the ejection half-cycle (Greco et al., 2013) as

$$U_0 = \frac{1}{\tau}\int_0^{\tau/2} u_c(t)\,\mathrm{d}t, \qquad \tau = \frac{1}{f}, \tag{1}$$

where $u_c(t)$ is measured on the actuator centreline one actuator diameter downstream of the exit. The corresponding fluidic power per actuator is estimated as in Gil & Strzelczyk (2016)

$$P = \frac{1}{2}\,\rho\, A\, U_0^3, \tag{2}$$

and remains approximately constant over the explored parameter range.
Since the reward is evaluated from planar EBIV measurements, unbalanced forcing normal to

the laser sheet could steer the jet axis out of the measurement plane and bias the reward. To avoid this artefact, we impose zero net forcing in the direction perpendicular to the laser plane by constraining diametrically opposed actuator pairs to operate with identical frequency and phase, specifically pairs (1,4) and (2,5) as labelled in Figure 1.

2.3. Bayesian optimisation

The actuation parameters are tuned using BO, a sample-efficient strategy for expensive and noisy black-box objectives (Garnett, 2023). In the present study, the input vector is $\mathbf{x} = [f_1, f_2, f_3, f_6, \Delta\phi_1, \Delta\phi_2, \Delta\phi_3] \in S \subset \mathbb{R}^7$, where f_i are the SJ actuation frequencies (with $f_1 = f_4$ and $f_2 = f_5$) and $\Delta\phi_i$ are the phase delays with respect to actuator 6 (with $\Delta\phi_4 = \Delta\phi_1$ and $\Delta\phi_5 = \Delta\phi_2$). At each iteration, a Gaussian Process (GP) surrogate $f(\mathbf{x}) \sim \mathcal{GP}(0, k)$ with an Radial Basis Function (RBF) kernel $k(\mathbf{x}, \mathbf{x}') = \sigma_f^2 \exp\big(-\|\mathbf{x} - \mathbf{x}'\|^2/(2\lambda^2)\big)$ is fitted to the data $\mathcal{D} = \{(\mathbf{x}_i, y_i)\}_{i=1}^n$, with observations $y = f(\mathbf{x}) + \epsilon$, $\epsilon \sim \mathcal{N}(0, \sigma_\epsilon^2)$. New candidates are selected by maximising the Expected Improvement (EI) acquisition function, which balances exploration and exploitation by favoring points with either low predicted cost or high predictive uncertainty.

2.4. EBIV processing and reward definition

Event data associated with each laser pulse are accumulated over a fixed time window to form pseudo-images, which are then processed with standard PIV algorithms to obtain time-resolved planar velocity fields (Willert, 2023). The pseudo-images are processed with an in-house multi-pass, multi-grid PIV routine, using a final interrogation window of 32×32 pixels^2 with 50% overlap. The camera is mounted with its short sensor side aligned with the jet axis to maximise the spanwise field of view, resulting in a measurement domain of approximately $1.5 < x/D < 3.1$ and $-1.6 < y/D < 1.6$. For each optimisation episode, a short event sequence is acquired, and only a subset of 500 pseudo-image pairs is randomly sampled and processed. The resulting velocity fields are then reduced to a scalar reward, enabling rapid evaluation of candidate control inputs while retaining a spatially resolved view of the flow response.

The measured two-component velocity field is denoted as $\boldsymbol{U} = [u, v]$, from which fluctuations $[u', v']$ are obtained by subtracting the episode-mean field. The ensemble-averaged TKE field is computed as

$$\overline{\mathrm{TKE}}(x, y) = \frac{1}{2}\left(\overline{u'^2}(x, y) + \overline{v'^2}(x, y)\right). \tag{3}$$

To promote mixing, the reward y is defined as the spatial average of $\overline{\mathrm{TKE}}$ over a region of interest Ω centred on the jet and restricted to energetic flow regions,

$$y = \frac{1}{|\Omega|}\int_\Omega \overline{\mathrm{TKE}}(x, y)\,\mathrm{d}\Omega, \qquad \Omega = \{(x, y) \mid \bar{u}(x, y) \geq 0.2\,\bar{u}_{\max}\}, \tag{4}$$

where $\bar{u}_{\max}$ is the maximum of the episode-mean streamwise velocity. This threshold mitigates spurious TKE inflation in low-signal regions, and yields a reward that is both physically meaningful and fast to compute from spatially resolved measurements.

To account for experimental variability, each episode is repeated twice. If the two reward evaluations differ by more than 3.5%, an additional repetition is performed and the final reward is computed as the average of the two closest values.

2.5. 3D-PTV experimental setup

Volumetric 3D-PTV measurements are performed to provide instantaneous, qualitative cross-checks of the flow response under selected actuation settings. The flow is seeded with $1\,\mu\mathrm{m}$ DEHS droplets and illuminated from below by a dual-cavity Nd:YAG laser (15 Hz, 200 mJ) shaped into an approximately $9\,\mathrm{mm}$-thick volume. Four 5.5 Mpx Andor Zyla sCMOS cameras are arranged in a rhombus (diamond) configuration around the jet, with one forward-scatter view ($f_{\#} = 16$), one backward view ($f_{\#} = 8$) and two side views ($f_{\#} = 11$). The reconstructed domain spans approximately $100 \times 80 \times 9\,\mathrm{mm}^3$ at ≈ 27, and acquisition frequency is $f_{\mathrm{PIV}} = 10\,\mathrm{Hz}$. Particle reconstruction and tracking are carried out with an in-house, MATLAB-based implementation of the advanced Iterative Particle Reconstruction (IPR) algorithm (Wieneke, 2012; Jahn et al., 2021), employing an optical transfer function (OTF) to improve the accuracy of the back-projection (Schanz et al., 2016). The raw images are pre-processed by eigenbackground removal to suppress the stationary background and reflections (Mendez et al., 2017). Finally, the reconstructed particle fields are re-centred using the jet axis identified on the uncontrolled case, so that all cases share a common reference frame.

3. Results

Figure 2 reports the evolution of the optimisation reward y_i over the experimental episodes i. The blue markers show the reward obtained for each evaluated actuation setting, while the red curve tracks the best value achieved up to a given episode. After an initial exploration phase (shaded region), the optimisation consistently identifies actuation settings yielding higher rewards, and the best-so-far value increases in discrete steps as new favourable regions of the parameter space are discovered.

Figure 3 illustrates how the optimisation navigates the actuation space by relating the evaluated control parameters to the achieved reward. For each actuator group, the light-blue markers report the actuation frequency, normalized as Strouhal number St, used in each episode (left axis), while the dashed blue curve shows the corresponding moving average, highlighting the dominant trend as the optimiser progresses. The phase delays $\Delta\phi$ are defined with respect to actuator 6 and are shown on the secondary axis by the grey/black markers; the dashed black curve indicates the moving average of $\Delta\phi$. Despite the exploratory scatter at low rewards, higher-reward outcomes pro-

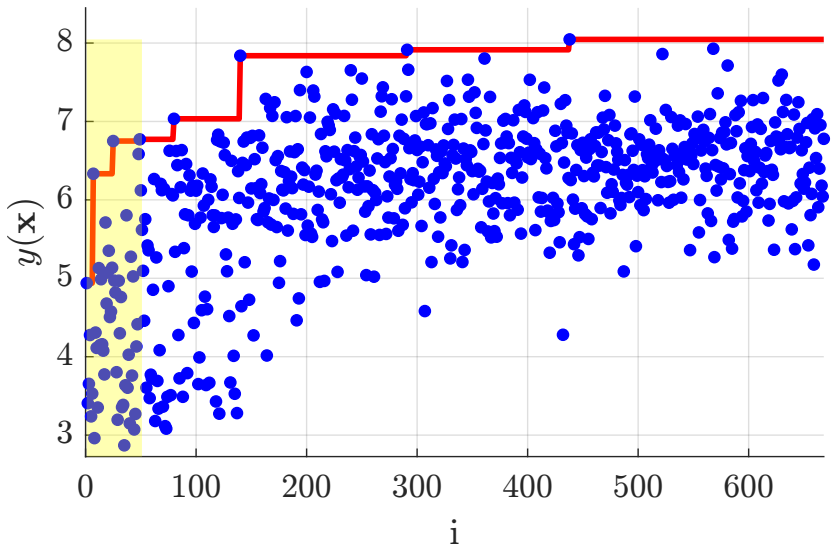

Figure 2. Evolution of the EBIV-derived reward y_i over optimisation episodes i. Blue markers: reward obtained for each evaluated actuation setting. Red line: best-so-far reward $\max_{k \leq i} y_k$. The shaded region indicates the initial exploration episodes used to seed the optimisation.

gressively concentrate around a narrower range of parameters. In addition, the moving-average curves reveal a systematic drift toward preferred forcing bands in terms of St (most evident for SJ-1 and SJ-2), whereas SJ-6 exhibits an opposite tendency, converging toward higher St at the highest rewards.

3.1. Mean flow and jet statistics

The three best-performing actuation cases, ranked according to the reward, are compared with the unforced jet using the time-resolved EBIV velocity fields. While only 500 randomly selected snapshots of the acquired event stream were processed during the optimization, the full acquisition record of 6000 snapshots is considered here. The velocity fields are computed using a multi-frame PIV correlation algorithm (Sciacchitano et al., 2012), providing improved accuracy and temporal resolution for the subsequent statistical analysis. Figure 4 reports the mean streamwise and transverse velocity, and Figure 5 the corresponding centreline-velocity decay and jet half-width b (defined from $\bar{u} = 0.5\,\bar{u}_c$). The unforced jet preserves its core across the field of view, with a nearly constant centreline velocity and a slightly contracting half-width typical of the near field. All controlled cases instead exhibit a faster centreline decay and a monotonic increase of b, consistent with enhanced spreading and mixing. The reward gain is quantified in Table 1: the spatially averaged TKE of the controlled cases exceeds that of the unforced jet by nearly an order of magnitude.

The table highlights a non-trivial result. Although the optimization aimed to maximize the TKE within the reward region, the statistics computed from the full multi-frame, time-resolved dataset reveal a slight mismatch with the optimization ranking. Specifically, the mean TKE obtained for Run 437 is lower than that of Run 567. This apparent inconsistency is likely related to the inter-

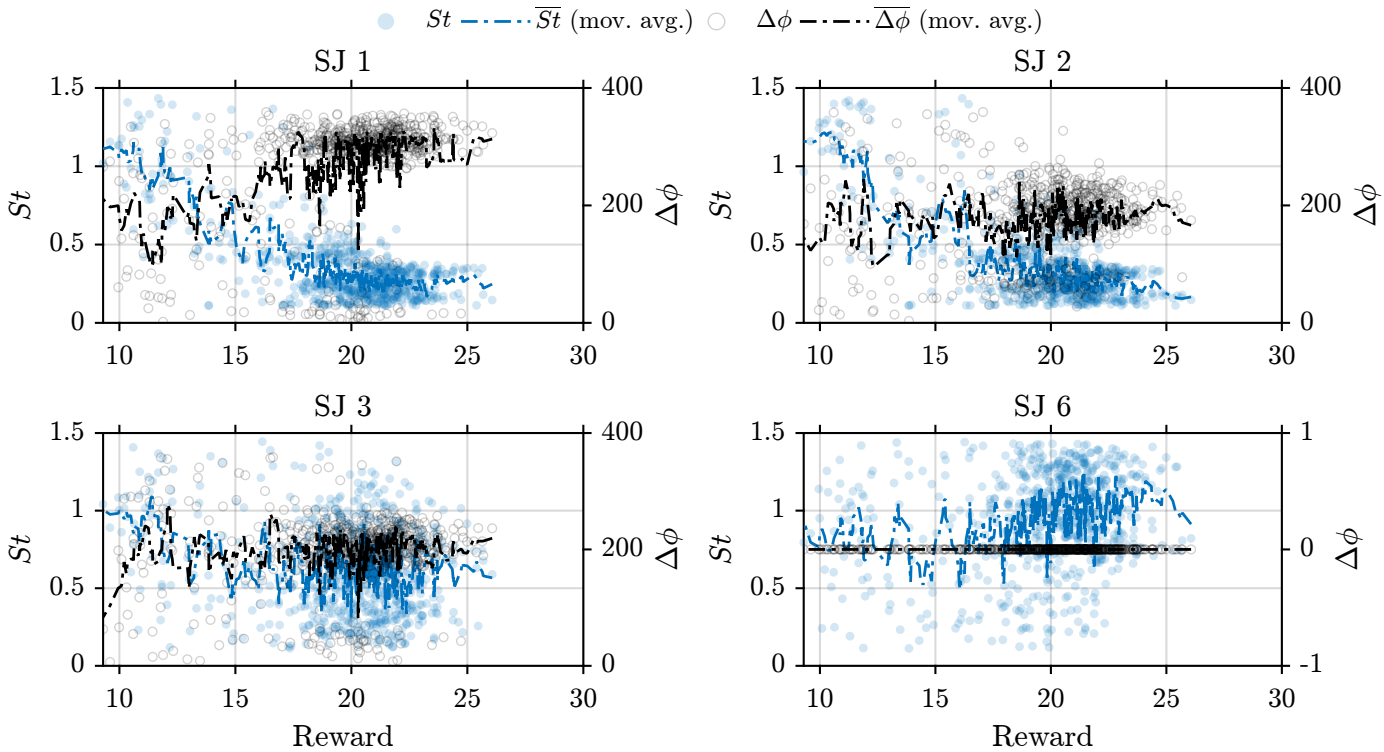

Figure 3. Actuation parameters versus achieved reward for each actuator group. Light-blue markers: actuation frequency, reported in Strouhal number St (left axis); dashed blue line: moving average of St. Grey/black markers: phase delay $\Delta\phi$ relative to actuator 6 (right axis); dashed black line: moving average of $\Delta\phi$.

mittency of the TKE field. Since the reward was evaluated from a limited subset of snapshots, the larger fluctuations associated with Run 437 may have produced a higher estimated reward during the optimization than the one obtained when averaging over the full record.

Another relevant observation concerns the relation between mixing and centreline velocity. Conventional jet-control optimisation has frequently adopted the minimisation of the centreline velocity as a surrogate objective for mixing, on the assumption that a faster centreline decay is equivalent to stronger mixing (Zhou et al., 2020; Shaqarin et al., 2024). The present EBIV-in-the-loop reward, defined directly on the TKE field, decouples these two objectives: the case with the lowest centreline velocity is the third-best by reward, whereas the highest-reward case retains a comparatively higher centreline velocity (Figure 5). The two surrogates are therefore not interchangeable, and a spatially resolved TKE reward, made affordable by the in-the-loop EBIV estimation, selects a different optimum than centreline-velocity minimisation would. We note that Table 1 also shows that the highest-reward case is not the one with the largest time-averaged TKE but the one with the strongest intermittent peaks, a distinction captured by the random-sampling reward estimator.

3.2. Coherent structures

The organization of the fluctuating velocity field is investigated through a Proper Orthogonal Decomposition (POD) of the time-resolved velocity fluctuations. Figure 6 shows the cross-stream

Table 1. Region-of-interest TKE statistics, normalised by U_b^2, for the unforced jet and the three best controlled cases (ranked by reward). Mean and peak refer to the time-averaged and instantaneous spatially averaged TKE over Ω.

case	$\overline{\mathrm{TKE}}_\Omega/U_b^2$	$\mathrm{TKE}_{\Omega,\mathrm{peak}}/U_b^2$	peak/mean
Uncontrolled	0.0047	0.029	6.3
Best (reward)	0.036	0.104	2.9
2nd best (reward)	0.038	0.084	2.2
3rd best (reward)	0.036	0.076	2.1

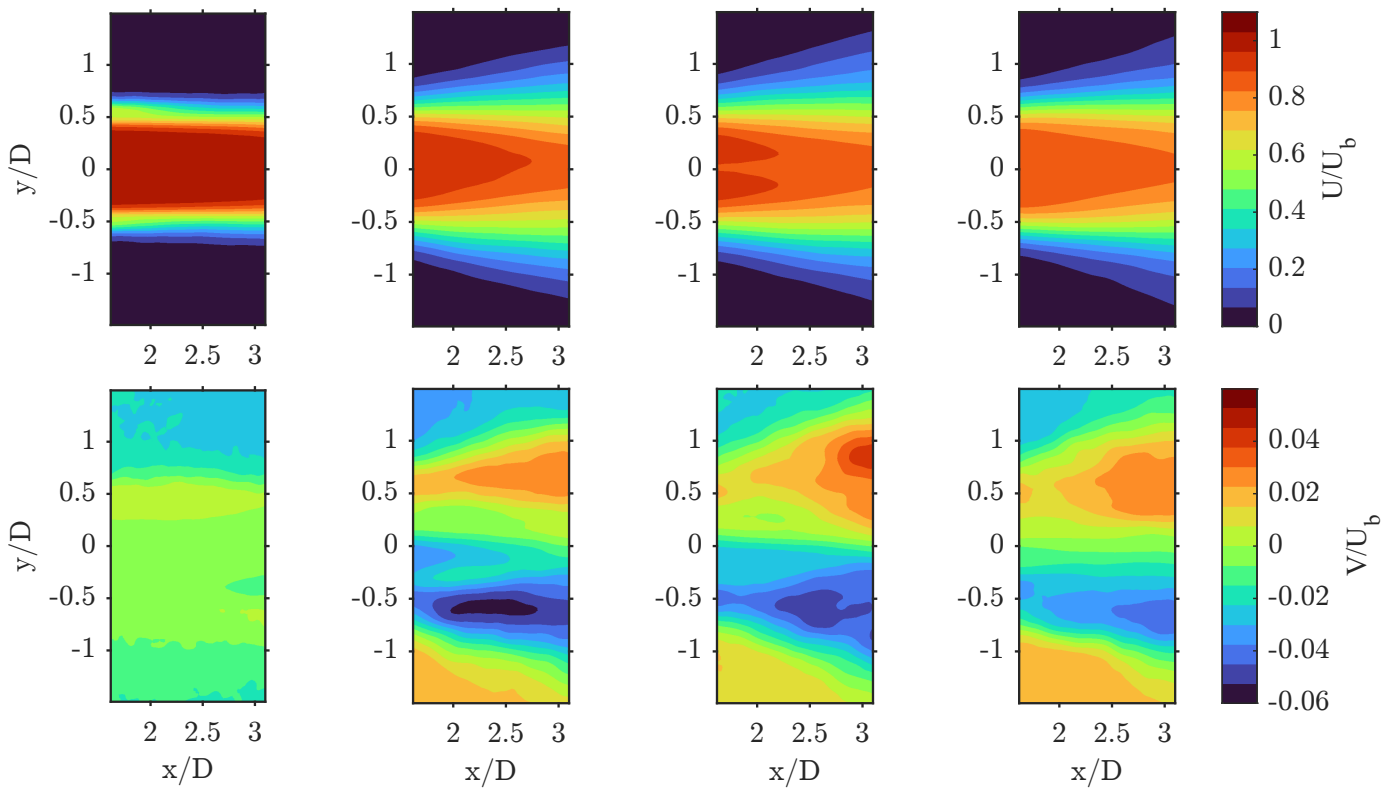

Figure 4. Mean streamwise (top) and transverse (bottom) velocity, normalised by U_b. Columns, left to right: unforced jet, best, second-best and third-best controlled case (ranked by reward).

velocity component of the two leading modes for the unforced jet and for the three selected controlled cases. In the unforced configuration, the leading mode pair exhibits a wavepacket-like pattern that becomes more pronounced toward the downstream part of the measurement domain. This behaviour is consistent with the development of Kelvin–Helmholtz-type structures associated with the natural jet-column dynamics. Under control, the dominant coherent organization changes depending on the actuation strategy. For the two highest-reward cases, the leading modes are dominated by broader, larger-scale structures, indicating a large-scale modulation of the jet. By contrast, the third-ranked control case exhibits more compact, shorter-wavelength structures, suggesting that the forcing promotes a response at smaller spatial scales. In all controlled cases, the first two modes appear spatially shifted in quadrature, which is consistent with advecting wave-like structures. The appreciable differences among the controlled modal shapes indicate that the

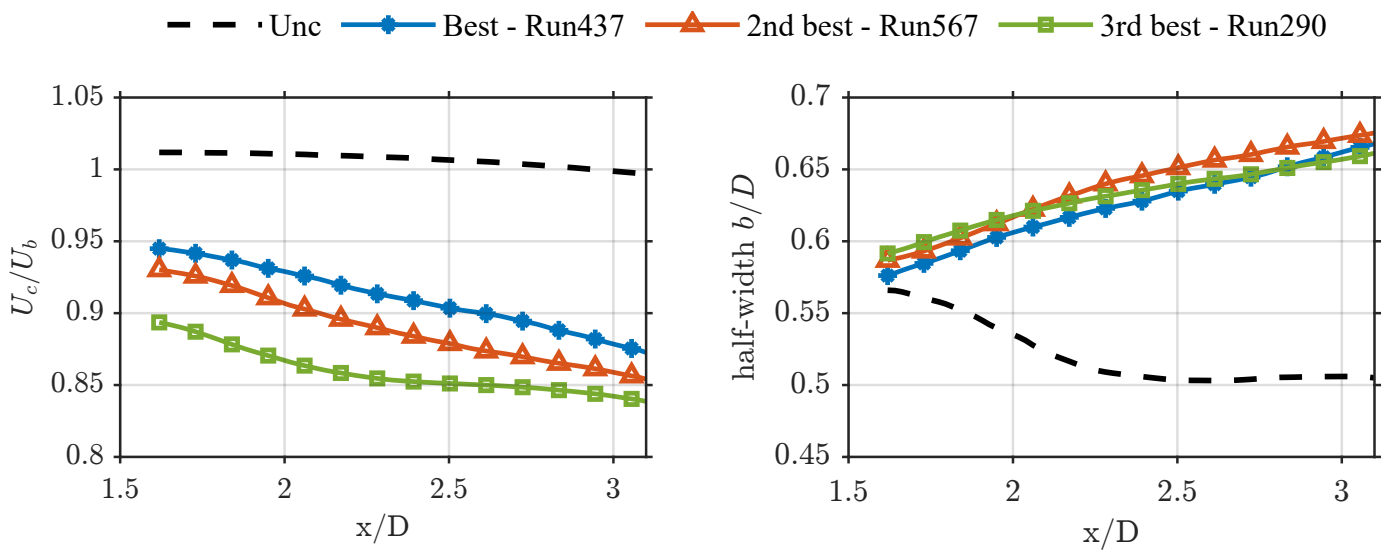

Figure 5. Centreline-velocity decay U_c/U_b (left) and jet half-width b/D (right) versus streamwise distance, for the unforced jet and the three best controlled cases (ranked by reward).

actuation does not simply amplify the natural jet mode, but introduces case-specific coherent structures.

3.3. Structure of the optimised actuation space

To visualise how the explored actuations relate to the achieved reward, the normalised parameter vectors are embedded in two dimensions by multidimensional scaling, preserving pairwise distances in the actuation space (Figure 7). The high-reward samples concentrate in a compact region of the embedding rather than at an isolated point, indicating a robust family of effective actuations. Colouring the embedding by the individual parameters shows that this region is organised primarily by the Strouhal numbers of the paired actuators (1,4) and (2,5), which tend to low values, while actuator 6 tends to higher St; the phase delays play a secondary role. This is consistent with the parameter trends of Figure 3 and provides a compact, interpretable picture of the optimum. Within this region, however, the best solutions are not all alike but realise qualitatively different actuation patterns, reflected in the distinct coherent structures of Figures 6 and 8. In particular, some of the most effective solutions appear to excite subharmonics of the dominant forcing, a known route to promote vortex pairing in the shear layer (Zaman & Hussain, 1980; Nekkanti et al., 2025). A systematic characterisation of these actuation patterns and of the associated mixing mechanisms is beyond the scope of the present conference contribution and is left to future work.

3.4. Instantaneous three-dimensional structure

Figure 8 shows instantaneous Q-criterion isosurfaces, coloured by velocity magnitude $|\mathbf{U}|$, for the unforced jet and the best and third-best controlled cases, computed from individual 3D-PTV snap-

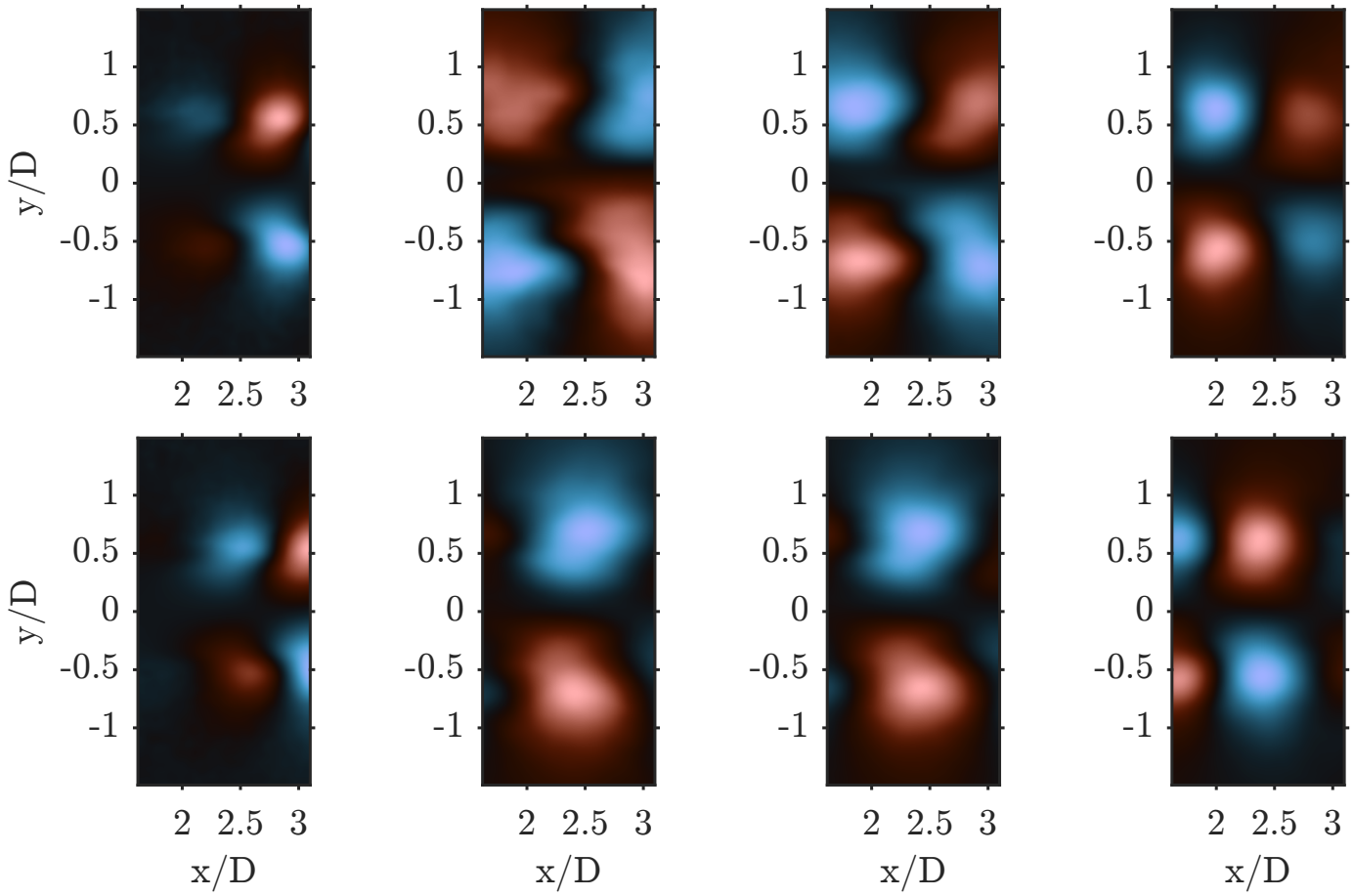

Figure 6. Cross-stream component of the two leading POD modes (top: mode 1, bottom: mode 2) for the unforced jet and the three best controlled cases (columns as in Figure 4).

shots interpolated onto a regular grid; the translucent mid-plane ($z = 0$) reports $|\mathbf{U}|$ for context. In the unforced jet, the high-speed core is almost unperturbed (the narrow high-$|\mathbf{U}|$ band along the axis) and carries a few large, coherent ring-like vortices generated by the Kelvin–Helmholtz instability of the shear layer. In the best case (Run437), the core is strongly attenuated and widened, and the vortical field breaks into numerous smaller, low-momentum structures spread across the volume, consistent with the faster centreline decay (Figure 5) and the intense intermittent peaks of the TKE reward found for this case (Table 1). The third-best case (Run290) presents an intermediate, steadier scenario, with fewer and more coherent annular vortices that retain their organisation as they convect, i.e. enhanced organisation rather than breakdown. This three-dimensional picture is consistent with the planar POD modes of Figure 6: the leading modes of the third-best case (Run290) are already more compact and spatially localised than those of the best case (Run437), and the volumetric Q-criterion reproduces the same trend. The agreement indicates that the planar EBIV measurement faithfully reflects the three-dimensional organisation of the flow, lending confidence to its use as the in-the-loop reward sensor.

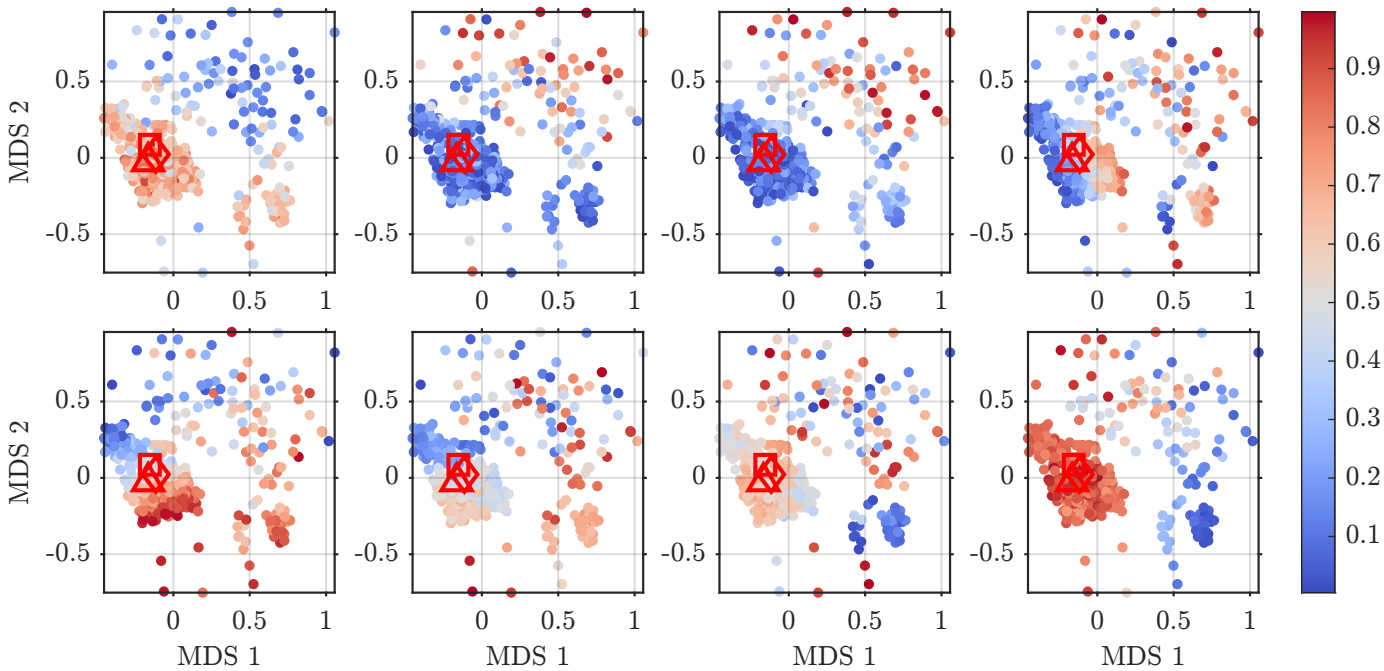

Figure 7. Two-dimensional multidimensional-scaling embedding of the explored actuation space (each panel is the same embedding), coloured by the achieved reward and by the individual normalised actuation parameters. Red markers (triangle, square, diamond) indicate the best, second-best and third-best case.

4. Conclusions and Outlook

This study shows that pulsed-EBIV can be effectively embedded within an experimental optimisation loop to evaluate complex, spatially resolved objective functions directly from velocity-field measurements. By leveraging the low latency and high sensitivity of event-based cameras under pulsed illumination, the approach enables time-resolved flow sensing with comparatively simple and non-intrusive instrumentation. The key advantage of the proposed framework is that the optimisation objective is no longer restricted to point-wise measurements or simple scalar surrogates, but can be constructed from spatial features of the instantaneous velocity field.

In the present work, this concept was demonstrated using Bayesian optimisation to identify effective actuation parameters for jet control. However, the EBIV-based sensing-and-evaluation framework is not intrinsically tied to Bayesian optimisation and could be integrated with other optimisation or learning strategies, including more complex algorithms requiring online evaluation of field-based reward functions.

Compared to traditional point-probe feedback, EBIV-based reward evaluation retains spatial information critical to assess global flow changes, while remaining sufficiently lightweight to support iterative optimisation over multiple actuation settings. The time-resolved fields further allow the optimised solutions to be characterised in terms of mean-flow statistics, coherent structures and a low-dimensional view of the actuation space. A notable outcome is that a spatially resolved TKE reward selects a different optimum than the centreline-velocity surrogate commonly used in

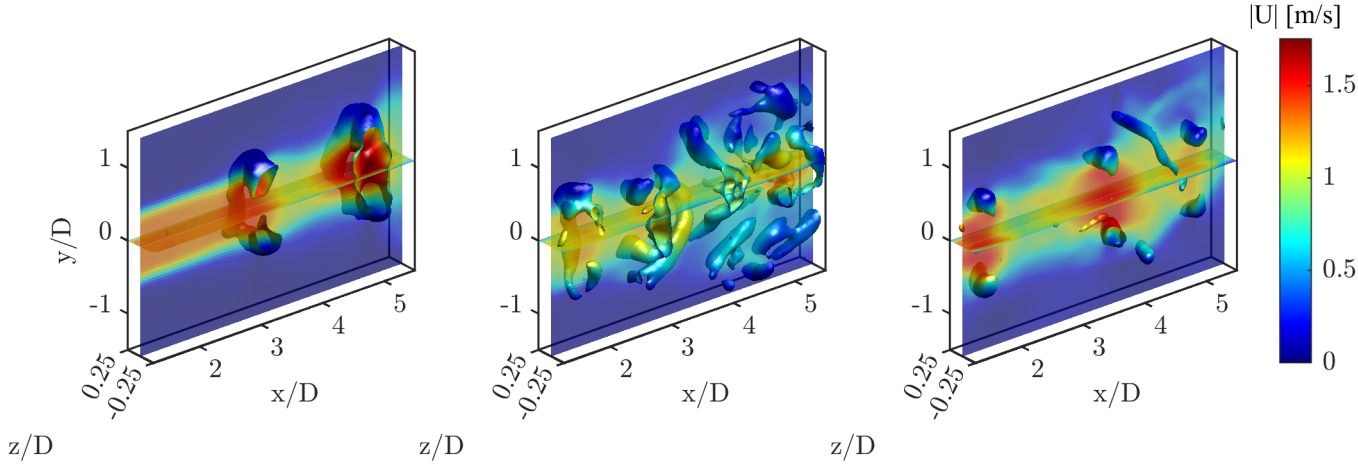

Figure 8. Instantaneous Q-criterion isosurfaces from single 3D-PTV snapshots, coloured by velocity magnitude $|\mathbf{U}|$; the translucent plane shows $|\mathbf{U}|$ at mid-span ($z = 0$). Left to right: unforced jet, best (Run437) and third-best (Run290) controlled case. Reported as a qualitative cross-check only: thin illuminated volume, non-time-resolved acquisition, single-snapshot gradients.

jet-control optimisation, highlighting the value of an in-the-loop, field-based objective. A more extended volumetric analysis, including flow statistics, is in progress and will further extend the present qualitative observations.

Acknowledgment

This project has received funding from the European Research Council (ERC) under the European Union's Horizon 2020 research and innovation program (grant agreement No 949085).

References

Gallego, G., Delbrück, T., Orchard, G., Bartolozzi, C., Taba, B., Censi, A., … Scaramuzza, D. (2022). Event-based vision: A survey. *IEEE Transactions on Pattern Analysis and Machine Intelligence*, *44*(1), 154-180. doi: 10.1109/TPAMI.2020.3008413

Garnett, R. (2023). *Bayesian optimization*. Cambridge University Press.

Gil, P., & Strzelczyk, P. (2016). Performance and efficiency of loudspeaker driven synthetic jet actuator. *Experimental Thermal and Fluid Science*, *76*, 163–174. doi: 10.1016/j.expthermflusci.2016.03.020

Greco, C. S., Ianiro, A., Astarita, T., & Cardone, G. (2013). On the near field of single and twin circular synthetic air jets. *International journal of heat and fluid flow*, *44*, 41–52. doi: 10.1016/j.ijheatfluidflow.2013.03.018

Jahn, T., Schanz, D., & Schröder, A. (2021). Advanced iterative particle reconstruction for lagrangian particle tracking. *Experiments in Fluids*, *62*(8), 179. doi: 10.1007/s00348-021-03276-7

Mendez, M. A., Raiola, M., Masullo, A., Discetti, S., Ianiro, A., Theunissen, R., & Buchlin, J.-M. (2017). Pod-based background removal for particle image velocimetry. *Experimental Thermal and Fluid Science*, *80*, 181–192. doi: 10.1016/j.expthermflusci.2016.08.021

Moreno, J. R., Franceschelli, L., De la Prida, D., Azpicueta-Ruiz, L. A., & Raiola, M. (2024). Implementation of a jet collector and dissipation cavity into a closed anechoic chamber for jet noise studies. In *30th aiaa/ceas aeroacoustics conference (2024)* (p. 3066). doi: 10.2514/6.2024-3066

Nekkanti, A., Colonius, T., & Schmidt, O. T. (2025). Nonlinear dynamics of vortex pairing in transitional jets. *Journal of Fluid Mechanics*, *1018*, A32.

Parekh, D., Kibens, V., Glezer, A., Wiltse, J., & Smith, D. (1996). Innovative jet flow control-mixing enhancement experiments. In *34th aerospace sciences meeting and exhibit* (p. 308). doi: 10.2514/6.1996-308

Schanz, D., Gesemann, S., & Schröder, A. (2016). Shake-the-box: Lagrangian particle tracking at high particle image densities. *Experiments in Fluids*, *57*(5), 70. doi: 10.1007/s00348-016-2157-1

Sciacchitano, A., Scarano, F., & Wieneke, B. (2012). Multi-frame pyramid correlation for time-resolved piv. *Experiments in fluids*, *53*(4), 1087–1105.

Shaqarin, T., Jiang, Z., Wang, T., Hou, C., Cornejo Maceda, G. Y., Deng, N., … Noack, B. R. (2024). Jet mixing optimization using a bio-inspired evolution of hardware and control. *Scientific Reports*(1).

Wieneke, B. (2012). Iterative reconstruction of volumetric particle distribution. *Measurement Science and Technology*, *24*(2), 024008. doi: 10.1088/0957-0233/24/2/024008

Willert, C. (2023). Event-based imaging velocimetry using pulsed illumination. *Experiments in Fluids*. doi: 10.1007/s00348-023-03641-8

Zaman, K., & Hussain, A. (1980). Vortex pairing in a circular jet under controlled excitation. part 1. general jet response. *Journal of fluid mechanics*, *101*(3), 449–491.

Zhou, Y., Fan, D., Zhang, B., Li, R., & Noack, B. R. (2020). Artificial intelligence control of a turbulent jet. *Journal of Fluid Mechanics*, *897*, A27. doi: 10.1017/jfm.2020.392